The Dependence of Numerically Simulated Convective Storms on Vertical Wind Shear and Buoyancy

M. L. WEISMAN AND J. B. KLEMP

National Center for Atmospheric Research,[1] Boulder, CO 80307

(Manuscript received 9 October 1981, in final form 2 February 1982)

ABSTRACT

The effects of vertical wind shear and buoyancy on convective storm structure and evolution are investigated with the use of a three-dimensional numerical cloud model. By varying the magnitude of buoyant energy and one-directional vertical shear over a wide range of environmental conditions associated with severe storms, the model is able to produce a spectrum of storm types qualitatively similar to those observed in nature. These include short-lived single cells, certain types of multicells and rotating supercells. The relationship between wind shear and buoyancy is expressed in terms of a nondimensional convective parameter which delineates various regimes of storm structure and, in particular, suggests optimal conditions for the development of supercell type storms. Applications of this parameter to well-documented severe storm cases agree favorably with the model results, suggesting both the value of the model in studying these modes of convection as well as the value of this representation in identifying the proper environment for the development of various storm types.

1. Introduction

Over the past 30 years, severe storm research has identified and described a wide range of convective storm types. These have been classified according to degree of severity (ability to produce hail, high winds, tornadoes), longevity, mode of propagation, intensity of rainfall and other related features. For certain types of storms, conceptual models have been proposed to describe the characteristic storm structures. Those most completely documented include the short-lived single cell (e.g., Byers and Braham, 1949), the discretely propagating multicell (Marwitz, 1972; Newton and Fankhauser, 1975), and the long-lived continuously propagating supercell (e.g. Browning, 1964; Lemon and Doswell, 1979). While these models provide an excellent basis for understanding the nature of certain storms, observations indicate enough variation and overlap of these types to suggest a more continuous spectrum of possible storm structures (e.g., Foote, 1977).

A hypothesis which is gaining both observational and theoretical support is that the spectrum of convective storm types may be dependent upon a relatively small number of observable parameters defining the environment in which the storms grow. Two of these parameters, namely parcel buoyancy (stability) and vertical wind shear, are believed to be particularly important in influencing storm evolution and structure. In the present study we shall investigate the dependence of storm characteristics on various magnitudes of buoyancy and wind shear through comparative simulations with a three-dimensional numerical cloud model. Other factors, such as synoptic or mesoscale forcing (Tripoli and Cotton, 1980; Schlesinger, 1982), may be equally important in influencing convective storm structure, but dealing with the many modes of forcing found in nature (thermal boundaries, terrain features, jet stream features, etc.) would greatly complicate this initial study. As such, this study is most applicable to convective storms which evolve in the absence of strong forcing features and does not address the question of storm initiation. For example, the current results may not be applicable for cases involving squall lines or warm and cold frontal boundaries, or cases in which nearby convective cells influence the development of a given cell. However, a large number of well-documented severe storm cases are characterized by relatively isolated convective cells which apparently are not strongly dependent on mesoscale or synoptic-scale features.

Several recent studies highlight the observational evidence linking storm structure to vertical wind shear and buoyancy. In a study of Alberta hailstorms, Chisholm and Renick (1972) identified characteristic wind hodographs associated with single-

[1] The National Center for Atmospheric Research is sponsored by the National Science Foundation.

0027-0644/82/060504-17$08.25

cell, multicell and supercell storms. These hodographs display a general increase in vertical wind shear as the storm type varies from single cell through supercell. The level of instability (buoyancy) indicated by the associated temperature and moisture soundings is comparable for the multicell and supercell regimes, and generally much larger than those for the single-cell regime. In cases where larger instabilities occur with small vertical wind shears, an additional disorganized multicell regime is identified.

Marwitz (1972a,b,c) similarly described multicell and supercell regimes and added an additional severely sheared regime. Again, vertical wind shear is found to increase in progressing from multicell, through supercell, to the severely sheared storm types. Multicell and supercell storms generally occurred in atmospheres with similar instabilities although multicells occasionally arose in more stable environments. Fankhauser and Mohr (1977) further documented these relationships in a study of northeastern Colorado hailstorms.

Although these results and others suggest the same general hierarchy of storm structures based on wind shear and buoyancy, uncertainties abound in attempts to quantify the relationships. These difficulties are caused, at least in part, by the large variability of conditions associated with observational data sets. For example, other factors important to storm growth, such as forcing, horizontal inhomogeneities, etc., may differ significantly from case to case. There is also a degree of subjectivity required in classifying the nature of particular storms. As noted by Foote (1977), many storms have characteristics appropriate to more than one class at any given time. Additional ambiguities arise owing to all the possible variations which are observed in vertical profiles of wind, temperature and moisture associated with severe convective events (e.g., Maddox, 1976).

In theoretical studies of convection, the importance of wind shear and buoyancy in determining certain storm features such as steadiness and propagation has been consistently noted (e.g. Moncrieff and Green, 1972; Moncrieff and Miller, 1976; Moncrieff, 1978). However, to avoid the intractability of the full equations of motion, these studies deal with simplified forms of convection and results apply to specialized storm structures such as two-dimensional squall lines (Lilly, 1979).

Three-dimensional numerical models which solve the equations of motion with parameterized physics provide more detailed descriptions of storm evolution, though questions remain in interpreting the realism of the simulated storms. In earlier numerical work, Pastushkov (1975) noted that strong vertical wind shear was detrimental to weakly buoyant convective elements while intensifying more buoyant elements. Storm intensification was maximized at an intermediate value of shear. Schlesinger (1978), Wilhelmson and Klemp (1978) and Klemp and Wilhelmson (1978a) have demonstrated a relationship between vertical wind shear and long-lived split storms, but did not systematically consider variations to the buoyant energy.

In this paper, we extend the earlier modeling work of Wilhelmson and Klemp (1978) and Schlesinger (1978) to study the effects of wind shear and buoyancy on storm structure over a wide range of environmental conditions. As part of this investigation, we seek to test the hypothesis that the evolution of supercell storms requires an overall balance between the magnitude of the wind shear and the amount of buoyant energy in the prestorm environment. This can be accomplished in a controlled setting within the three-dimensional cloud model by fixing the initial and environmental conditions and then selectively varying certain of these conditions. Of course uncertainties still arise in trying to relate the model simulations to real storms, but the recent success of models in reproducing many of the observed features of severe storms provides some confidence in the viability of this approach (e.g. Klemp and Wilhelmson, 1978b; Klemp, *et al.*, 1981; Wilhelmson and Klemp, 1981).

As discussed in Section 2, model storms are initiated in a horizontally homogeneous environment characterized by vertical profiles of temperature, moisture and wind which are consistent with observed conditions in the neighborhood of severe storms. Total parcel buoyancy and vertical wind shear are varied over a prescribed range, forming a two-dimensional convective parameter space in which storm structure and evolution can be studied. The results suggest a hierarchy of model storm types which is qualitatively similar to those observed in nature. The influence of vertical wind shear on storm evolution is discussed in Section 3, and extended to include the effects of variations in buoyancy in Section 4. Finally, in Section 5 we will characterize the above relationships in terms of a nondimensional convective parameter defined as a ratio of buoyancy to wind shear. This convective parameter is then calculated for several well-documented severe storm cases to investigate the applicability of these results to observed storms.

2. Experimental procedures

The basic tool for these sensitivity experiments will be the three-dimensional cloud model formulated by Klemp and Wilhelmson (1978a), with modifications described by Chen (1980). Some of the key features include use of the fully compressible equations of motion, a Kessler-type parameterization for the microphysics, and a turbulence parameterization in

which mixing coefficients are derived from a turbulence energy equation. Also, open lateral boundaries allow time-varying transports through the boundaries of the domain. At the present time, the model does not include ice processes.

The numerical simulations are initiated in a horizontally homogeneous atmosphere which contains an axially symmetric thermal perturbation of horizontal radius 10 km and vertical radius 1400 m. A temperature excess of 2°C is specified at the center of the thermal (located 1400 m AGL) and decreases gradually to 0°C at its edge. The magnitude of this perturbation represents the minimum value necessary to produce consistent development of an initial convective cell within the experimental range of environmental conditions. In order to test the sensitivity of this initialization procedure, several experiments were run in which the size of the bubble and the magnitude of the temperature excess were varied over a wide range of conditions. It was found that such changes can have a pronounced quantitative effect on the initial storm growth, but have less of an effect on subsequent storm redevelopments. For any initial perturbation used, however, the qualitative relationships of storm structure versus wind shear and buoyancy remain intact.

The horizontal domain size is 40 km × 60 km with a constant mesh interval of 2 km. Finer resolution would be preferable, but impractical for the large number of experiments necessary to complete the parameter study (>80 experiments including sensitivity studies). A representative set of experiments, however, were conducted using a 1 km horizontal mesh and confirmed to a large degree the results for the 2 km simulations. In particular, the storm evolutions were qualitatively the same, but the scale of the storm features were reduced by up to 30% in the 1 km experiments (see also Klemp *et al.*, 1981). The vertical domain extends to 17.5 km with a vertical mesh interval which stretches smoothly from 350 m at the lowest grid point to ~1 km at the top of the domain (Chen, 1980). This stretching scheme improves the numerical resolution near the surface, where it is most needed, without the expense of increasing the total number of grid points.

The vertical profiles of temperature, moisture and wind speed used in the simulations are defined by analytic expressions designed to provide smooth data profiles which can be altered by varying appropriate coefficients. The environmental potential temperature $\bar{\theta}$ and relative humidity H are given by

$$\bar{\theta}(z) = \begin{cases} \theta_0 + (\theta_{tr} - \theta_0)\left(\dfrac{z}{z_{tr}}\right)^{5/4}, & z \leqslant z_{tr} \\ \theta_{tr} \exp\left[\dfrac{g}{c_p T_{tr}}(z - z_{tr})\right], & z > z_{tr} \end{cases} \quad (1)$$

$$H(z) = \begin{cases} 1 - \dfrac{3}{4}\left(\dfrac{z}{z_{tr}}\right)^{5/4}, & z \leqslant z_{tr} \\ 0.25, & z > z_{tr} \end{cases} \quad (2)$$

where z_{tr} = 12 km, θ_{tr} = 343 K and T_{tr} = 213 K represent the height, potential temperature and actual temperature, respectively, at the tropopause and θ_0 = 300 K is the surface potential temperature. The mixing ratio is kept constant at a maximum value q_{v0} near the surface to approximate a well-mixed boundary layer. These profiles are depicted in Fig. 1.

For the purposes of this paper, buoyancy is defined as the positive energy available to a parcel rising from the surface through the extent of the cloud, i.e.,

$$B = g \int \frac{\theta(z) - \bar{\theta}(z)}{\bar{\theta}(z)}\, dz, \quad (3)$$

where $\theta(z)$ defines the moist adiabatic ascent of a representative surface parcel and the integral is taken over the vertical interval where the lifted parcel is warmer than its environment (positive area on a skew T). Buoyancy is varied by altering the magnitude of q_{v0}, which changes the parcel ascent profile given by $\theta(z)$. The values of q_{v0} chosen range from 11 through 16 g kg^{-1} and their associated parcel ascent curves are illustrated in Fig. 1. The positive energy as calculated in (3) for the values of q_{v0} range from ~1000 m^2 s^{-2} to ~3500 m^2 s^{-2}. Variations in buoyancy could also have been achieved by changing the temperature profile. Future experiments will consider such modifications more completely, but initial tests suggest the qualitative results to be insensitive to at least small changes in the above profile.

Some of the more significant features of the thermodynamic profile are the fairly well mixed boundary layer (constant mixing ratio, almost constant θ), a low LCL (lifted condensation level), and a moist adiabatic parcel ascent characterized by from 0.5 to 3°C negative buoyancy at cloud base and from between 4 and 10°C of buoyancy at 500 mb (depending on the value of q_{v0}). Above the mixed layer, the relative humidity decreases steadily with height, but no attempt is made to reproduce the midlevel dry intrusion which is often observed in severe weather situations. It is felt that this feature would complicate these characterizations and should be considered separately in a future experiment. Otherwise, this basic sounding is within the range of observed soundings associated with severe weather occurrences (e.g., Fawbush and Miller, 1954; Fankhauser and Mohr, 1977).

The wind profile chosen for the simulations is formulated to approximately preserve the depth of the shear layer while varying the magnitude of the shear proportional to the parameter U_S, i.e.,

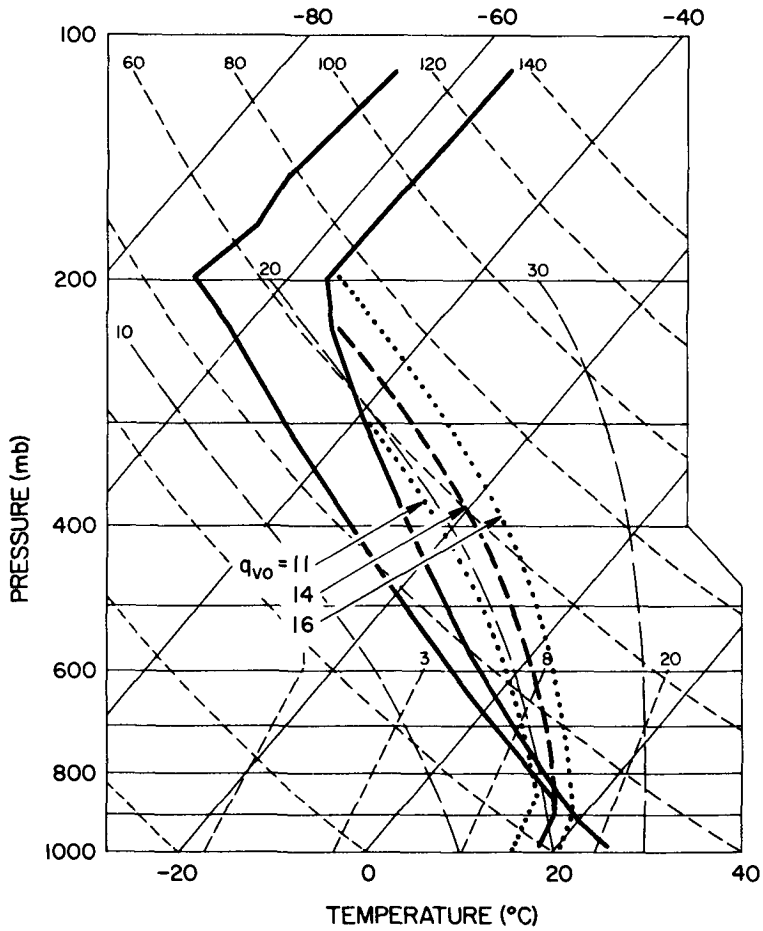

FIG. 1. Skew T diagram depicting temperature and moisture profiles used in model experiments (heavy solid lines). Heavy dashed line represents a parcel ascent from the surface based on a surface mixing ratio q_{v0} = 14 g kg^{-1}. Heavy dotted lines represent similar parcel ascents for q_{v0} = 11 g kg^{-1} and 16 g kg^{-1}. Tilted solid lines are isotherms, short dashed lines are dry adiabats, and long dashed lines are moist adiabats.

$$U = U_S \tanh z/z_s , \quad (4)$$

where z_s = 3 km is kept constant through all the simulations. U_S is varied from 0 through 45 m s^{-1} and when viewed as an average wind shear over the first 6 km, covers the entire range of shears considered by Marwitz (1972); i.e. an average shear of 0–0.008 s^{-1}. These wind profiles are depicted in Fig. 2. Shear is confined to the lower portion of the troposphere based on the results of Wilhelmson and Klemp (1978) which suggested that low-level shear is more important to the development of modeled supercell structures than upper level shear. A one-directional shear profile (i.e., a straight line hodograph) is used because it simplifies some interpretations of the storm dynamics for these experiments, and it allows one to make use of the symmetry properties of the model equations to reduce the computation domain by one-half. With the Coriolis force omitted, the model simulation is symmetric about a vertical east-west plane through the center of the

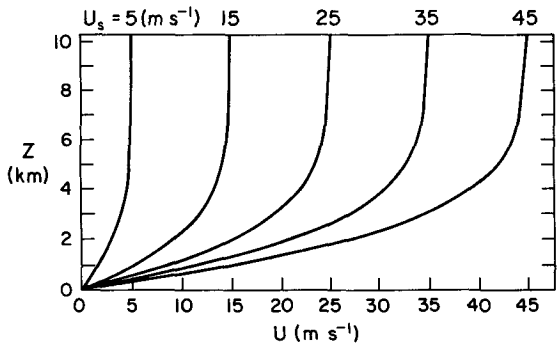

FIG. 2. Wind profiles as defined by Eq. (4).

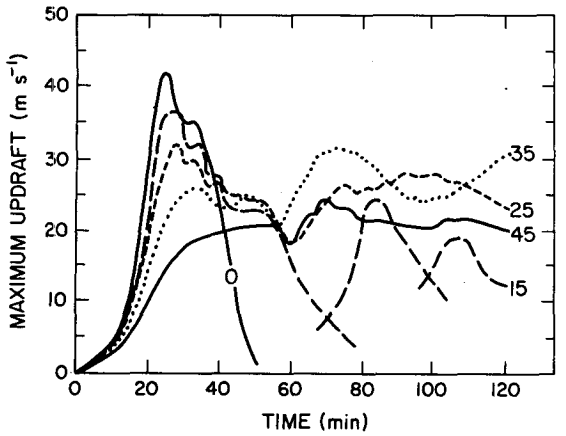

FIG. 3. Time series of maximum vertical velocities for the U_S = 0, 15, 25, 35 and 45 m s^{-1} wind shear experiments. q_{v0} = 14 g kg^{-1}.

initial buoyant region, parallel to the wind shear vector. For the current simulations, only the southern half of the domain is simulated and presented.

3. Wind shear experiments

For the following set of experiments, the surface mixing ratio, q_{v0}, is held constant at 14 g kg^{-1}. Storms are initialized for the range of wind profiles plotted in Fig. 2 and allowed to evolve through 2 h. The resulting variations in storm evolution and structure display a hierarchy qualitatively similar to the one observed in real storms.

The nature of the wind shear, storm structure relationship is reflected in the time series plots of maximum vertical velocity w presented in Fig. 3. During the initial 50 min of model simulation, each storm evolves through a cycle of growth (due to the initial buoyant plume) followed by decline (due to water loading, rainout, etc.), with the maximum strength of the initial updraft decreasing steadily with increasing shear. This adverse effect of wind shear is consistent with the findings reported by Byers and Braham (1949), and is predominantly due to the increased entrainment experienced by storms growing in more strongly sheared environments. These entrainment effects are also evidenced by an increasing downshear tilt of the initial updraft (axis of maximum W) with increasing shear and a drop in the temperature excess experienced in the core of the initial updraft from 9 to 6.5°C as U_S varies from 0 through 45 m s^{-1} (a 9°C temperature excess corresponds closely to that based on undiluted moist adiabatic ascent).

In the case of no vertical wind shear, a rain-evaporation induced cold surface outflow develops by 40 min into the simulation and spreads axisymmetrically away from the storm. This effectively cuts off the warm inflow to the updraft and the storm continues to decline. By 70 min into the simulation, the storm has dissipated. This is the model equivalent to observed short-lived isolated cells as discussed by Byers and Braham (1949).

With increasing environmental shear, however, storm redevelopment occurs over much of the wind shear range tested, as indicated by the updraft strengths after 50 min in Fig. 3. Two modes of redevelopment seem to dominate the results. In the first mode distinct new cell development occurs along the boundary of the storm-induced cold outflow near the surface (Chen, 1980). In the second, storms split into a rightward and leftward self-sustaining pair as described by Wilhelmson and Klemp (1978) and Schlesinger (1980). Both of these modes of redevelopment are characterized by a more erect or slightly upshear tilting updraft as opposed to the downshear tilt which characterized the initial buoyant plume.

Horizontal cross sections presented in Figs. 4–6 for the U_S = 15, 25 and 35 m s^{-1} experiments, respectively, illustrate the key features of the different storm evolutions. In order to keep the storms nearly stationary in the center of the domain, a mean storm speed in the direction of the shear (determined by trial and error), $\bar{U}$, has been subtracted from the wind field at the beginning of each simulation. Thus, the depicted wind vectors are approximately storm relative except for propagation in the cross-shear direction. Note also that only the southern half of the symmetric domain is presented, the northern half being a mirror image.

Distinct new cell development along an outflow boundary is found to occur within the low to moderate range of our wind shear experiments. This is exemplified by the U_S = 15 m s^{-1} simulation (Fig. 4). By 40 min of model simulation the initial updraft (storm 1) has already weakened from a maximum of from 38 to 25 m s^{-1} due to water loading. Rain has just begun to reach the ground and the gust front, which divides the warm relative inflow and the colder outflow, is already positioned 10 km east of the parent storm. The supply of potentially warm air necessary for sustaining the updraft is thus effectively cut off and the updraft continues to weaken. Surface convergence is strongest on the right and left flanks of the storm but as the surface outflow increases in strength, convergence along the gust front becomes strongest directly downshear (east) of storm 1, where the outflow is in direct opposition to the shear-induced inflow. By 80 min, this convergence has developed a new cell (storm 2) 10 km east of storm 1, just ahead of the existing surface rain field. This second storm is again fed by the warm air ahead of the gust front and achieves a maximum updraft intensity of 23 m s^{-1} just after 80 min. It then begins a similar decline due to water loading and rainout and the gust front continues to progress eastward

relative to the updraft core. By 2 h a third updraft has intensified to 13 m s^{-1}, but remains weaker than the initial redevelopment (see Fig. 3). After 2 h the system steadily decays.

The almost periodic nature of this redevelopment process is dependent upon the ability of the surface gust front to both move ahead of an existing cell (thereby cutting off the warm inflow to the updraft) and then to trigger and sustain new cell growth along the outflow boundary. The second stage of this process is sensitive to both the thermodynamic characteristics of the environment in which the gust front propagates (which determines how much lifting the inflow air needs before it becomes buoyant) as well as the speed at which the gust front propagates relative to the newly developing cell (which influences the time over which inflow can be supplied to the new updraft). Thus, if the low-level environment is too stable for the amount of lifting available, or if the gust front moves too quickly away from a developing cell, successive redevelopment will not occur.

Many of these features are characteristic of observed multicell storms. Organized multicells, however, frequently evolve through cell growth on the right flank rather than on the forward flank and evolve through many more than the two or three cycles in the above simulations. Thorpe and Miller (1978) and Chen (1980) have been more successful in reproducing both of these observational features with similar speed wind shear conditions, but also with directional variation of the environmental wind shear vector. The above simulations do not include such directional shear, but further research is currently underway to determine the influence of curvature of the wind shear vector on multicell storm propagation. For the present, we will refer to the storm redevelopment with U_S = 15 m s^{-1} as the "secondary storm".

As the vertical wind shear is further increased, secondary cell redevelopment is replaced by a regime of storm splitting. This process is described in detail by Wilhelmson and Klemp (1978) and Schlesinger (1980) and differs from the weaker shear case in that redevelopment now occurs in a relatively continuous fashion on both the right and left flanks of the original storm's outflow boundary. This produces two equal, self-sustaining storms which appear to propagate continuously to the right and left of the mean shear vector. The rightward moving storm possesses a cyclonically rotating updraft at midlevels while the leftward mover possesses an anticyclonically rotating updraft.

These features are evident in the U_S = 25 m s^{-1} experiment (Fig. 5) where we view the evolution of the right member of the split pair. By 40 min into the model simulation, rain has again reached the ground downshear of the storm's center and the resultant cold outflow has effectively cut off the warm relative inflow from the storm's forward flank. The updraft is weakening and the maximum vertical velocity has already shifted away from the symmetry axis at both low and midlevels, in conjunction with the maximum surface convergence. By 80 min, the right moving storm is progressing steadily south at ~6 m s^{-1} and has regained most of its initial strength. The updraft remains almost directly above the surface gust front and the warm relative inflow is able to continually sustain its existence. The storm maintains its strength through 2 h as it continues to progress southward along the gust front. By 2 h, an additional updraft has developed along the symmetry axis in the manner described for the secondary storms, but is much weaker than in the U_S = 15 m s^{-1} experiment.

A similar storm splitting is observed when U_S is increased to 35 m s^{-1} (Fig. 6), but various features of the storm structure and evolution change significantly. One of the more noticeable changes is the lack of any westerly storm relative surface outflow during any phase of the storm's evolution. The surface convergence along the forward flank of the initial gust front has likewise lessened and is now too weak to produce any sort of secondary cell redevelopment. However, the split storm updraft now becomes stronger than the initial cell (32 m s^{-1} vs 25 m s^{-1} in Fig. 3), suggesting that the increased shear is enhancing split storm development while still adversely affecting the initial storm development. As the wind shear is increased even further (for U_S = 45 m s^{-1}) redevelopment due to storm splitting still occurs, but the steadily increasing effects of entrainment weaken both the initial cell and split cell development. In more extreme shear cases, initial storm development may be stopped altogether.

The model-produced split storms possess many of the observational characteristics of observed supercells, including rightward propagation, a self-sustaining nature and, as will be shown below, preferred storm rotation (mesocyclone). Observations, however, rarely show an equal right and left moving pair, as is the case with these experiments (the left mover would be found in the northern part of the symmetric domain). Klemp and Wilhelmson (1978b) have shown that, ignoring the Coriolis force, a one-directional (straight line) hodograph will produce an equal right and left moving pair of storms (as in the present case) while a clockwise or counterclockwise curvature in the wind hodograph will favor the right or left moving storm, respectively. In the much more common severe weather case of a clockwise curved hodograph, the left mover may be very weak or apparently absent while the right mover is observed to be a classic supercell. In this respect, each of our modeled pair of "supercells" is similar to the often observed single rightward moving supercell.

An important aspect of both the secondary and split type of storm redevelopments is the relationship of the storm speed (motion of main updraft) to the surface gust front speed. In the present simulations, the speed of propagation of the gust front relative to the storm decreases in the down shear and cross shear direction as the vertical wind shear increases. At low shears (U_S = 15 m s^{-1}) the gust front propagates away from the storm in all directions while at high shears (U_S = 35 m s^{-1}) the gust front propagation may be the same as the storm propagation.

It appears as if a necessary condition for the development of the steady split storms is that the storm relative inflow be strong enough to keep the outflow from propagating away from the updraft. If the outflow is too strong, the gust front may move ahead of the storm and the supply of warm air to the updraft may be cut off. This would lead to a decline in storm strength and a loss in the storm's steadiness. In contrast, secondary storms appear to develop best when the outflow is slightly stronger than the inflow. This allows for a periodicity in redevelopment in which the decline of an older storm coincides with the triggering of a new storm downshear along the surface gust front (as shown in Fig. 4).

Rotational characteristics also differ noticeably between the secondary and split type of storm developments. Rotation evolves in the split-storm updrafts which is principally cyclonic in the rightward moving member and anticyclonic in the left member. On the other hand, no preferential rotation is noted in the secondary storms. The development of preferred rotation is apparently linked to the ability of the split storms to continuously sustain themselves, but the detailed mechanisms are as yet not well understood. However, evolution of vorticity in a simplified representation of a right moving storm has been discussed in detail by Rotunno (1981). In that study, it is suggested that a combination of the tilting and stretching terms in the vertical vorticity equation can explain many of the details of the vorticity evolution.

The generation of vertical vorticity in the present experiments is very similar to that described by Rotunno (1981) and by Wilhelmson and Klemp (1981). Some features of this vorticity evolution are summarized here in order to clarify some of the various storm structures described earlier. For this purpose, midlevel (4.6 km) vertical vorticity is plotted in Fig. 7 for the U_S = 15, 25 and 35 m s^{-1} experiments at

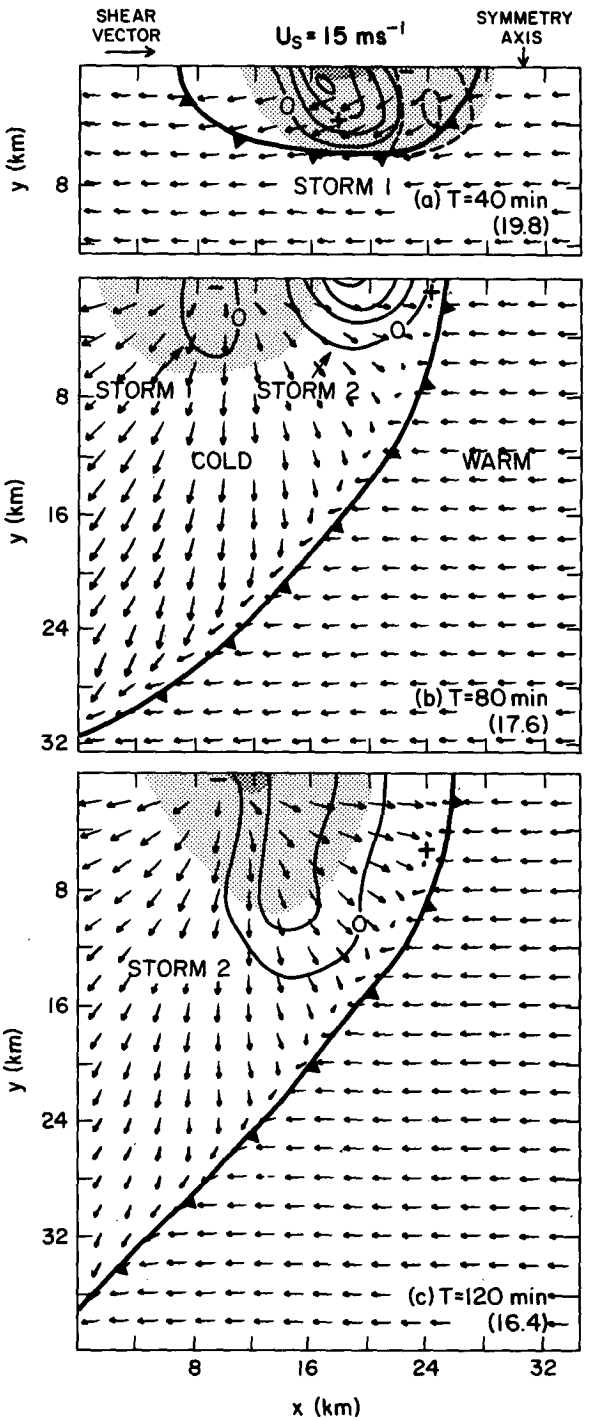

FIG. 4. Horizontal cross sections of storm features for the U_S = 15 m s^{-1}, q_{v0} = 14 g kg^{-1} experiment at (a) 40 min, (b) 80 min and (c) 120 min into the model simulation. Vectors represent storm relative low-level (178 m) horizontal winds (a mean storm speed $\bar{U}$ = 12 m s^{-1}, was subtracted from the initial field). The maximum vector magnitude is shown in parentheses in the lower right corner of each plot. The surface rain field is indicated by light stipling with rain areas >4 g kg^{-1} designated by dark stipling. The surface gust front is denoted by the solid barbed line and represents the −0.5°C temperature perturbation contour. The midlevel (4.6 km) vertical velocity field is contoured every 5 m s^{-1} for positive values and 2 m s^{-1} for negative values. The zero contours outside the main region of storm activity have been deleted. Plus and minus signs represent the location of the low-level (178 m) vertical velocity maximum and minimum, respectively.

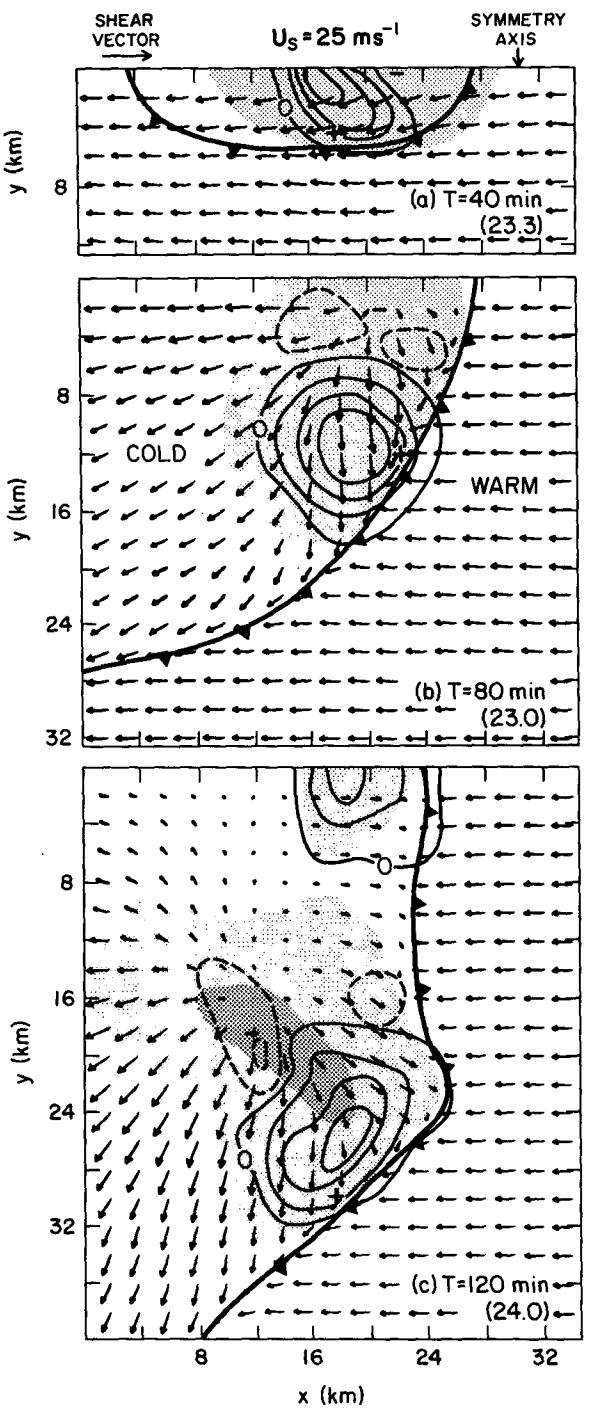

FIG. 5. As in Fig. 4, for U_S = 25 m s^{-1}, $\bar{U}$ = 19 m s^{-1}.

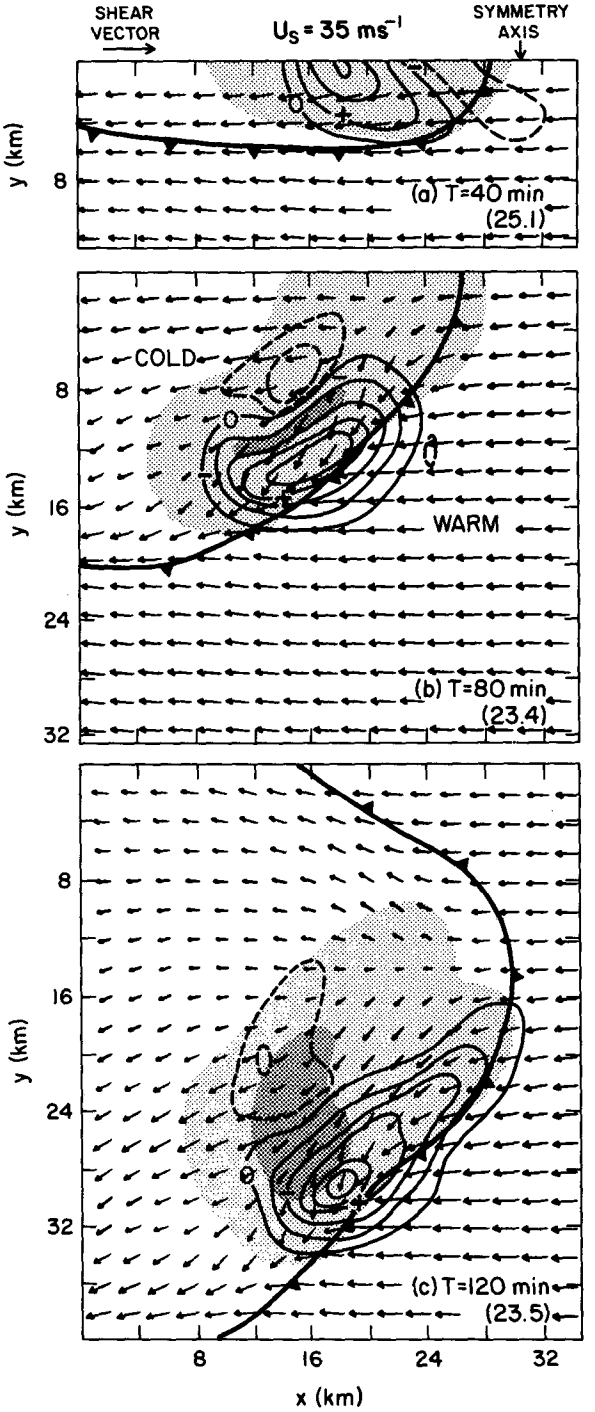

FIG. 6. As in Fig. 4, for U_S = 35 m s^{-1}, $\bar{U}$ = 22.5 m s^{-1}.

30 and 80 min into the model simulation. Also, time series plots of the maximum and minimum mid and low level vertical vorticity for the U_S = 15, 25, 35 and 45 m s^{-1} experiments are presented in Figs. 8a and 8b, respectively. As before, only results for the southern half of the symmetric domain are presented.

During the first 30 min of storm growth, midlevel vertical vorticity develops as a vortex couplet associated with the initial updraft. This is apparent in Fig. 7 which displays the cyclonic member of the vortex pair. Note that this vortex couplet occurs for all the shear experiments shown, but the magnitude

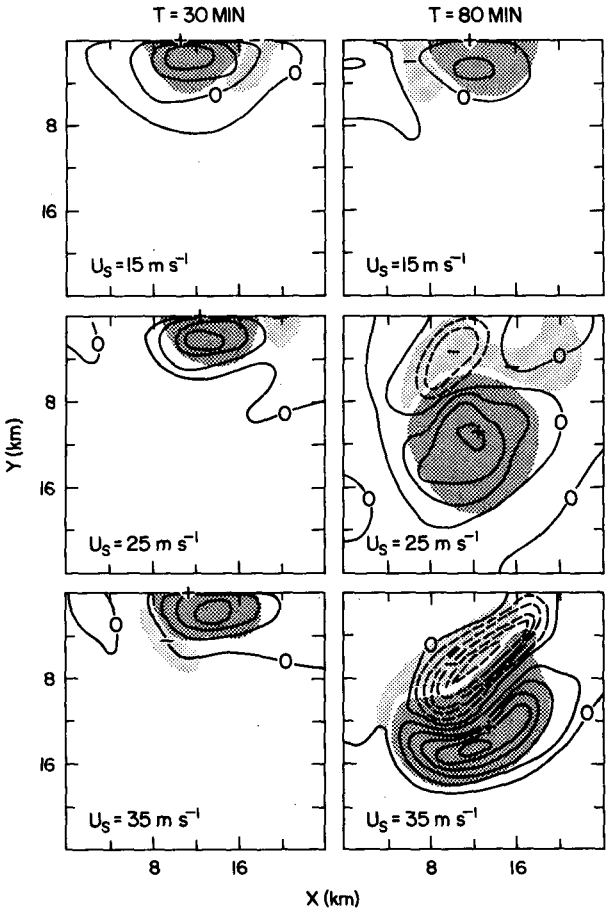

FIG. 7. Horizontal cross sections of midlevel (4.6 km) vertical vorticity for U_S = 15, 25 and 35 m s^{-1} at 30 and 80 min into model simulations. Vertical vorticity is contoured in units of 20 × 10^{-4} s^{-1}. Regions of positive and negative vertical velocity are indicated by the dark and light stipling, respectively, and the plus and minus signs indicate the location of the vertical velocity maximum and minimum. q_{w0} = 14 g kg^{-1}.

of the vorticity is maximized for the U_S = 35 m s^{-1} experiment (Fig. 8a). This is consistent with vorticity generation through tilting which produces vertical vorticity (in the form of a couplet) in proportion to the cross-shear horizontal gradient of vertical velocity and the magnitude of the shear. During the initial 30 min of these simulations, the magnitude of the vertical velocity is found to decrease as the shear increases (refer to Fig. 3). Thus, as the contribution to vorticity production due to shear is increasing, the contribution due to the gradient of vertical velocity is decreasing, thereby leading to the apparent maximum in vertical vorticity noted above.

After 30 min, the midlevel vorticity weakens along with the weakening initial updraft. In the split storm cases (U_S = 25, 35 and 45 m s^{-1}) the vorticity soon recovers and becomes stronger than for the initial storm. This recovery is associated with the intensification of the split storm updraft which, as shown in Fig. 7, has become preferentially aligned with the positive member of the original vortex pair (for the southern member of the split). During this phase of storm evolution, the magnitude of the vorticity clearly increases with increasing shear (Fig. 8a). Strong midlevel negative vorticity later develops in association with the split storm downdraft. This correlation of positive and negative vorticity with the updraft and downdrafts, respectively, in the split storms maintains itself until the storms finally decay. However, in the case of the secondary storm devel-

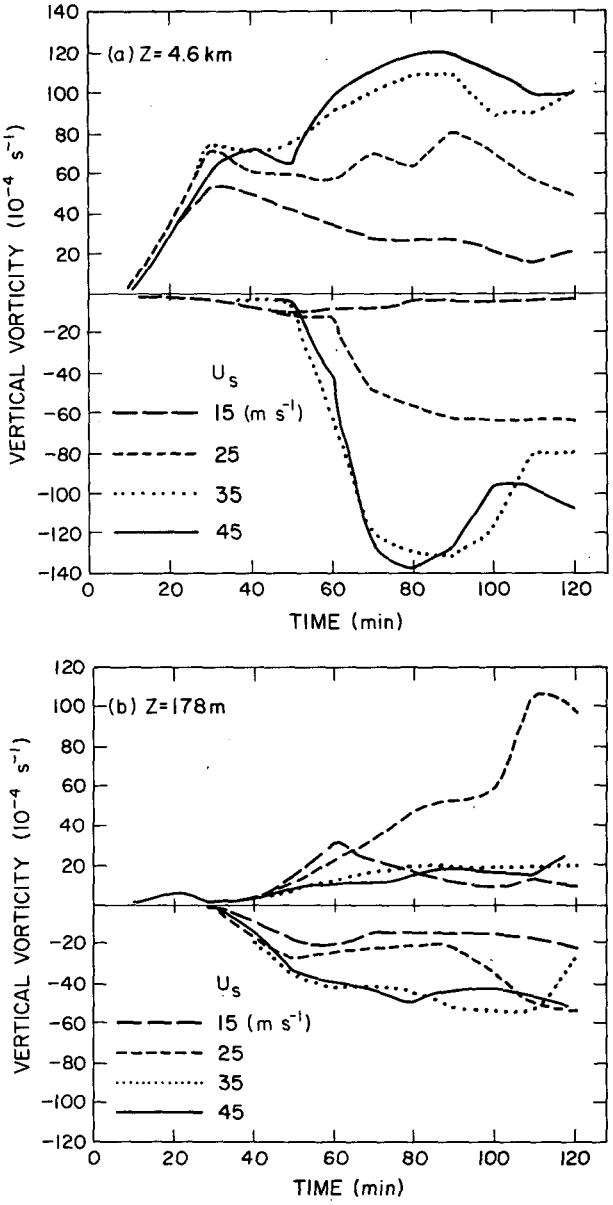

FIG. 8. Time series cross section of (a) midlevel (4.6 km) and (b) low-level (178 m) vertical vorticity extrema for the U_S = 15, 25, 35 45 m s^{-1} model experiments.

opment in the $U_S = 15$ m s^{-1} experiment, new updraft development merely produces new vortex couplets similar to that in the original updraft.

While the production of significant midlevel vorticity commences quite early in the life of the model storms, significant surface vorticity does not develop until ~40 min into the model simulations (Fig. 8b). This coincides with the development of the cold surface outflow, which suggests that increased convergence along the gust front is important in enhancing the low-level vorticity. For example, the strong convergence along the outflow boundary can enhance vertical vorticity production by tilting (owing to increased horizontal vertical velocity gradients) as well as by stretching.

A significant feature in Fig. 8b, though, is that the magnitude of the positive surface vorticity is strongly maximized in the $U_S = 25$ m s^{-1} experiment. The question of why such an optimal condition should exist is as yet unresolved, but the fact that one does exist in the model experiments has many implications. In particular, the existence of a strong low-level mesocyclone (vertical vorticity maximum) is closely related observationally to the development of tornadoes.

While the current model simulations have much too coarse a resolution to simulate actual tornado development, one may still compare some of the storm-scale features produced in the model to characteristic observed features of tornadic storms. For this purpose, we present in Fig. 9 some results for a 1 km horizontal resolution simulation with $q_{v0} = 14$ g kg^{-1} and $U_S = 30$ m s^{-1}. It is found that the 1 km simulations produce overall storm features which are more similar to observations than the 2 km simulations used above, but the difference in resolution does not significantly affect the results already presented. However, while the low-level vorticity production in the 2 km simulations is maximized for the $U_S = 25$ m s^{-1} experiment, low-level vorticity production in the 1 km simulations is maximized for $U_S = 30$ m s^{-1}. For comparison, we also present in Fig. 9 a representation of observed supercell storm features as described by Lemon (1980).

Note the position of the bounded weak echo region (BWER) and the hook structure relative to one another in the radar reflectivity field for the Lemon observational model and the coincidence of the hook structure in the rainwater field, positive vertical vorticity and updraft for the numerical simulation. Observationally, a hook structure and BWER have been associated with midlevel cyclonic rotation within the storm's updraft and the occurrence of tornadoes at the ground (e.g., Lemon and Doswell, 1979). The near coincidence of cyclonic rotation and upward motion at midlevels in the modeled split storms was apparent in Fig. 7, and here the coincidence of the hook structure and maximum vertical vorticity at low

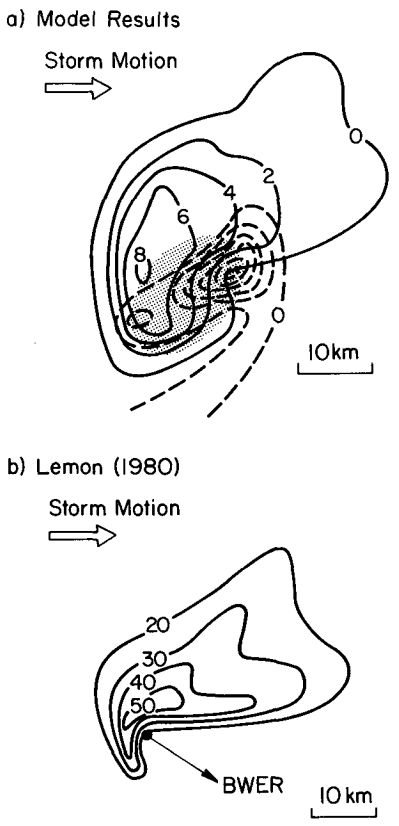

FIG. 9. Comparison of (a) modeled supercell storm features and (b) observed supercell storm features as suggested by Lemon (1980), showing (a) surface (178 m) rainwater contours every 2 g kg^{-1} (solid lines), surface positive vorticity field contoured in units of 20×10^{-4} s^{-1} (dashed lines), midlevel 4.6 km updraft > 10 m s^{-1} (stipling) and (b) low-level radar reflectivity contours [dB(Z)] and the location of the bounded weak echo region (BWER) at midlevels in the storm. (Note that only part of the Lemon picture has been reproduced to simplify the comparison.)

levels in the modeled storms is also apparent. Also note the good comparison between the radar reflectivity contours and rainwater contours, both showing the largest gradients in the right rear quadrant of the storm, in association with the hook structure.

It is clear from the previous discussions that secondary and split type developments in the model simulations are quite distinct both in appearance and in apparent dynamical structure. Furthermore their dependence on wind shear is at least qualitatively similar to the modes of convection observed in nature, i.e., multicells occur at relatively lower shears than supercells. Also, while the equivalence between the modeled secondary and split type storms and the observed multicell and supercells is by no means exact, enough similarities exist to suggest that the model is able to simulate at least the qualitative aspects of the supercell and multicell modes of convection. In the next section the dependence of these model storm structures on variations in the buoyant

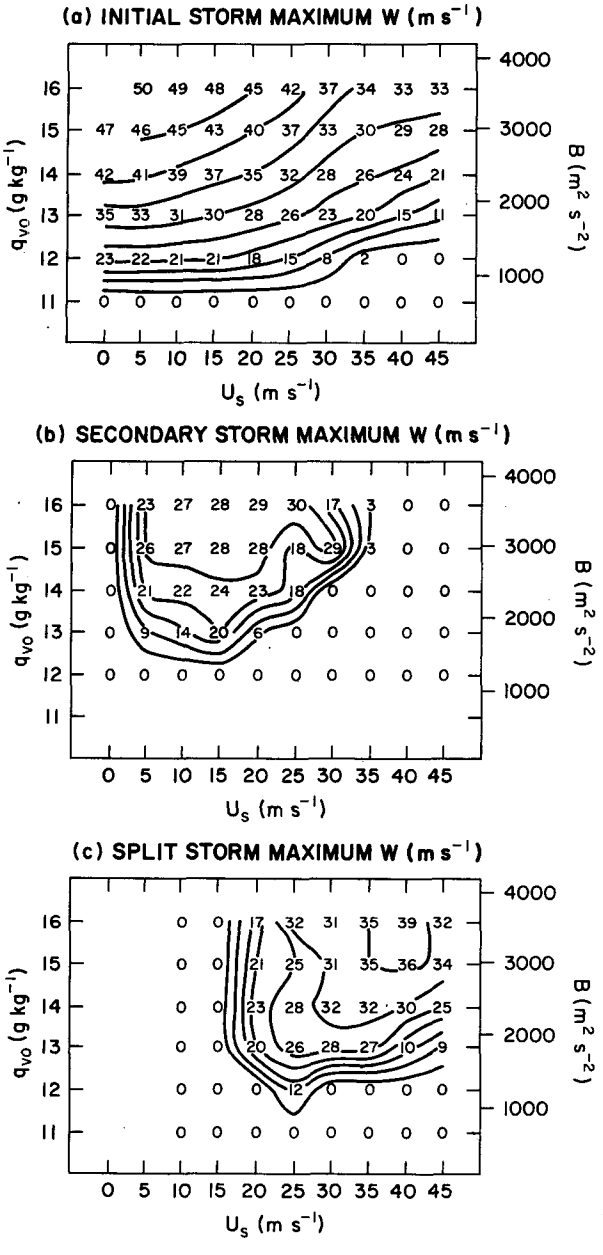

FIG. 10. Maximum vertical velocity (m s^{-1}) for (a) initial storms, (b) secondary storms and (c) split storms, plotted versus buoyant energy and vertical wind shear. Buoyant energy is given in units of both q_{v0} and B. Vertical wind shear is given in terms of U_S.

energy in the storm's environment will be included in this analysis.

4. Combined wind shear and buoyancy experiments

The amount of buoyancy available to a storm strongly modulates the influence of wind shear on storm structure through its impact on the overall intensity of convection. This intensity influences the surface outflow strength which affects both the amount of convergence along the gust front and its propagation relative to a given cell. These gust front characteristics strongly modulate the tendency to trigger new cells or produce splitting. Variations in the updraft strength also directly affect the production of storm rotation through both the tilting and stretching terms in the vertical vorticity equation. Such rotation is apparently linked to the process of storm splitting. Variations in updraft strength further modify storm evolution by altering the magnitude of entrainment processes.

In the following set of experiments, the buoyant energy is altered by varying the magnitude of the low-level environmental moisture as described in Section 2. Together with the variations in wind shear, conditions favoring various storm types can be identified. These conditions are summarized in Figs. 10–12 in which storm characteristics are plotted as a function of buoyancy (represented by q_{v0}) and wind shear (represented by U_S). Buoyancy is also plotted in terms of B, the total convective available potential energy [see Eq. (3)]. For the initial and secondary storms, plotted zero values imply that an updraft did not penetrate past the lowest levels of the model, although weak updrafts (<2 m s^{-1}) may occur in association with the initial perturbation or gust front convergence. For split storms, zero values represent cases where an updraft was unable to maintain its strength for at least 10 min as it progressed rightward (leftward) off the symmetry axis.

Fig. 10 depicts the maximum vertical velocity obtained in the initial convective cell which occurs at ~30 min into the simulation. As expected, the storm strength increases in magnitude with increasing buoyant energy and decreases with increasing vertical shear. The threshold buoyancy required to sustain moist convection for the given initial impulse corresponds to $\sim q_{v0} = 12$ g kg^{-1} for weak shear but increases with increasing wind shear. Thus, increasing vertical shear inhibits the initial storm growth for all levels of buoyant energy.

Fig. 10b represents the maximum vertical velocity attained in any secondary cell redevelopment of the initial cell as described in the previous section. The regime in which this redevelopment occurs is characterized by high buoyancy and low to moderate shear. With increasing buoyancy, the strengths of the new storms increase and they are able to form at higher shears. This is due in part to the decrease in surface convergence necessary to trigger a new cell as the surface moisture is increased (less negative area to overcome in the lower portion of the sounding). However, we believe the more important factor is the balance which apparently must exist between the storm relative inflow and storm-induced surface outflow to permit such redevelopments. As mentioned in the previous section this occurs when the gust front propagates downshear from the initial cell

(but not too rapidly). As the buoyancy increases, the strength of the downdraft outflow also increases. This effect may be counteracted by increasing the vertical wind shear, which effectively increases the storm relative inflow. Thus, the balance between low-level inflow and outflow which permits secondary redevelopments can occur at higher shears for higher buoyant energies. Note in Fig. 10b, however, that strong wind shear will suppress secondary type redevelopments completely, even at very high buoyancies.

The maximum vertical velocities obtained in the right (and left) moving split storms are depicted in Fig. 10c. This supercell regime occurs only at moderate to high shears with maximum intensities occurring along a diagonal axis of increasing buoyancy and wind shear. There is also an overlap region apparent at the lower shears where both split and secondary type storms are able to develop simultaneously (refer also to Fig. 10b). A similar overlap in storm types is noted in the simulations of Wilhelmson and Klemp (1981). The existence of an optimal balance between wind shear and buoyancy for supercell development is apparently again caused by the evolving balance between the downdraft outflow and storm relative inflow which, in this case, prohibits downshear propagation of the gust front relative to the storm. This optimal balance may additionally be influenced by the tradeoff between the enhancement of storm organization by developing strong rotational characteristics, and the destructive influences of entrainment. These competing effects are both influenced by the magnitudes of the buoyancy and wind shear.

The regime for significant positive low-level vorticity production (Fig. 11) coincides closely to the regime for split storms with the axis of maximum vorticity leaning toward higher shears for higher buoyancy. Notice that the region of maximum low-level vorticity occurs at lower shears than the region

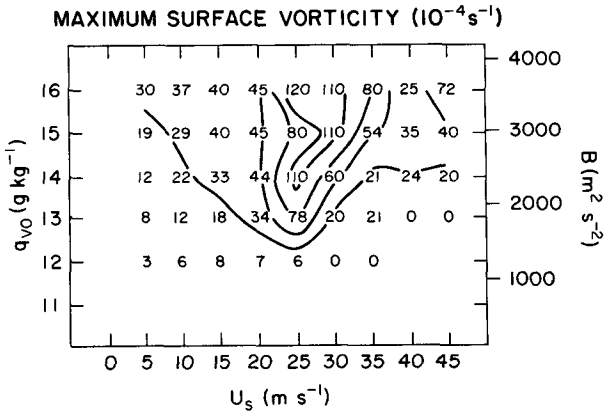

FIG. 11. As in Fig. 10 for maximum low-level (z = 178 m) vertical vorticity.

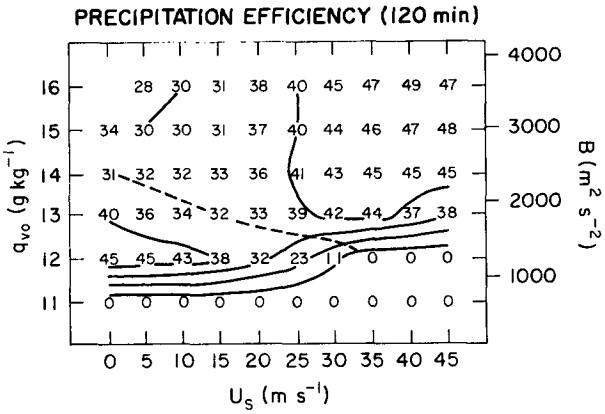

FIG. 12. As in Fig. 10, for precipitation efficiency (%).

of maximum split storm updraft intensity (Fig. 10c). We believe that the ability of the storm's relative downdraft outflow to maintain a strong downshear component behind the gust front is an important factor influencing the generation of positive low-level vertical vorticity (compare the orientations of outflow in Figs. 5c and 6c).

Precipitation efficiency is a parameter which has been frequently estimated in observational studies to characterize overall rain production. Definitions of this parameter vary, but generally include some measure of the total rainfall measured at the ground divided by the total water vapor flux into the storm. While this calculation requires numerous approximations for observed storms, it can be computed unambiguously within the model experiments. For this purpose, we equate the total moisture influx into a storm with the total condensation within the modeled storm and the total rainfall at the ground to the total flux of rain through the model's lowest grid point. The resulting precipitatioin efficiencies through 2 h of model integration time are shown in Fig. 12. Note that this calculation is not taken over the complete lifetime of a storm (model storms continue to survive past 2 h), but does encompass the mature stage of storm development. We would expect even higher precipitation efficiencies if computed over the storm's entire life, due to increased rainout and little new condensation during the dissipation phase.

Two regimes seem evident in the model results (separated by a dashed line). The first occurs at low buoyancies and low to moderate shears where there is little tendency for storm activity beyond the initial convective cell. Here, precipitation efficiencies decrease with increasing wind shear which is consistent with enhanced evaporation due to increased entrainment. The second regime covers the rest of the experimental range and exhibits generally increasing precipitation efficiency with wind shear and buoyancy. Much of this regime is associated with the development of split storms as indicated in Fig. 10c.

The observational results presented by Browning (1977) and others, however, indicate a decrease in precipitation efficiency with increasing shear, even for the supercell type storms considered. Clearly, more research is needed to interpret these results, especially in light of the considerable uncertainty inherent both in the observational calculations and in the microphysical representation within the model.

5. A nondimensional convective parameter

The dependence of the modeled storm structure on environmental buoyancy and wind shear can be consolidated and generalized in terms of a nondimensional parameter which combines these two effects. For this purpose, we have chosen a form of bulk Richardson number similar to the one proposed by Moncrieff and Green (1972) in an analytical study of two-dimensional convection, i.e.,

$$R = \frac{B}{\frac{1}{2}\bar{u}^2}, \tag{5}$$

where B [called convective available potential energy (CAPE) by Moncrief and Green] is defined by Eq. (3) and $\bar{u}$ represents a difference between the environmental wind speeds at low and midlevels. Surface parcel ascent in the calculation of B is based on a 500 m mean temperature and moisture value for the particular sounding.

The denominator is a measure of the low-level wind shear, but, for dimensional arguments, it can also be viewed as a measure of the inflow kinetic energy made available to the storm by the vertical wind shear. The latter interpretation was suggested by Moncrieff and Green, but in the present context, the two are essentially the same. To see this, one must merely assume that a consistent measure of wind shear is the difference between the actual storm motion, which represents an integrated effect of the shear profile, and a representative surface layer wind. In a storm relative framework, the magnitude of the shear [$\bar{u}$ in Eq. (5)] is then identical to the storm relative surface inflow, and thus, the denominator represents an inflow kinetic energy. For the present experiments, it was found that the storm motion in the direction of the shear was most comparable to a mean taken over the lowest 6 km of the shear profile. Thus, for computational purposes, $\bar{u}$ is defined to be the difference between a density-weighted mean wind speed taken over the lowest 6 km of the profile and an average surface wind speed taken over the lowest 500 m of the profile. In general, the depth over which such means are taken will vary depending upon the details of the particular wind profiles.

The numerator is clearly a measure of potential updraft strength but is also indirectly a measure of potential downdraft and surface outflow strength (i.e., the updraft produces water loading and the subsequent rainwater produces a downdraft and surface outflow). The denominator, as a measure of wind shear, represents both the strength of the surface inflow which feeds the storm and the ability of the updraft to take on the rotational characteristics seemingly necessary for the storm's organization. R, therefore, represents the relative balance of certain factors thought to be important in controlling storm structure and evolution.

Many limitations arise, however, in interpreting storm characteristics based on this single parameter. First, the buoyancy calculation as formulated does not consider the vertical distribution of buoyancy and, in particular, the negative contributions which are often observed near cloud base in severe storm situations (e.g., Fankhauser and Mohr, 1977; Browning, 1977). This negative buoyancy may limit the ability of a storm to regenerate itself along its outflow boundary or may help organize convection by favoring inflow into the larger, more established convective cells at the expense of smaller nearby cells. The buoyancy calculation also does not include the vertical distribution of moisture in the sounding. For example, it has long been suggested that the entrainment of midlevel dry air can enhance storm surface outflow through increased evaporational cooling. Entrainment of midlevel dry air can also decrease storm strength by decreasing the buoyancy in the cloud's updraft.

Another obvious restriction in the formulation of R is that the measure of wind shear does not consider the important effects of directional turning of the wind shear vector. As has been discussed previously, such curvature in the wind hodograph is usually noted in soundings associated with severe weather and low-level clockwise hodograph curvature seems instrumental in the production of observed supercell type storms. The detailed distribution of vertical shear is also not considered in defining R, although it may have significant influence on storm development.

In spite of these ambiguities, it is worthwhile to consider this parameter within the current experiment where R can be consistently calculated within the controlled environments. The buoyant energy is calculated for the experimental range of surface moisture values in Fig. 1 as described above and $\bar{u}$ is calculated for the range of profiles in Fig. 2. Fig. 13 displays a measure of storm strength S as a function of the parameter R. S is defined as the maximum vertical velocity obtained in a particular storm normalized by the maximum which would have occurred based solely on moist adiabatic parcel ascent, i.e.,

$$S = \frac{W_{\max}}{(2B)^{1/2}}, \tag{6}$$

where B is given by (3).

Initial storm strength is plotted versus R in Fig. 13a. Note the strong correlation in the results from experiments with differing values of q_{v0}. The only major exceptions are the low moisture $q_{v0} = 12$ g kg^{-1} cases where the initial warm bubble was barely strong enough to develop any initial updraft. The rapid decline of S at low values of R reflects the detrimental effect wind shear has on the growth of the initial buoyant plume, with storm development stopped altogether for $R < 8$. Of course, the actual value of this minimum threshold is to a large degree a function of the initial forcing. Another influencing factor would be the amount of moisture at midlevels in the sounding, which directly affects the impact of entrainment on the developing updraft. For example, a sounding which is significantly drier than that in Fig. 1 will not support as strong an initial updraft as in the present cases. The lower limit of R would therefore shift towards higher values. For large R, S seems to asymptotically approach a limiting value of ~0.6, suggesting that for the no-shear model simulations a maximum of 36% of the convective available potential energy in the soundings is directly converted to vertical kinetic energy, the rest being used to counter the effects of water loading, entrainment, adverse pressure gradients, etc. This ratio, though, may also be a function of both the initial forcing and the degree of moisture in the sounding.

Secondary storm strength versus R is plotted in Fig. 13b. The correlation among the experiments is still quite good (except for $q_{v0} = 13$ g kg^{-1}) and suggests that secondary type storms will not occur for $R < 35$. S remains fairly constant at a value of 0.35 within much of the permissible R range, but does show signs of decreasing at very large values of R (especially note the results for the 13 g kg^{-1} experiments). As R approaches infinity (i.e. no vertical shear), S approaches zero.

Split storm strength (Fig. 13c) again shows good correlation among experiments with optimal conditions occurring for R between 15 and 35. This would be the model range for supercell type development. For $R < 10$, the shear is too strong to permit storm growth, while for $R > 50$, buoyancy is too strong relative to the shear to allow the necessary balances which produce strong split storms.

In order to compare these results to observations, R has been calculated for the documented storms listed in Table 1. $\bar{u}$ is calculated as for the one directional shear profiles, except that now $\bar{u}$ is replaced by $\bar{u} + \bar{v}$, where u and v are the usual wind components and each mean is computed separately. This mean is not so clear a measure of the shear as it was in the one-directional case since it does not include the effects of hodograph curvature, but it does represent a simple, consistent method for measuring $\bar{u}$ over a wide variety of conditions. For each case in Table 1, a storm classification has been assigned as suggested in the documentation (i.e., multicell, supercell, . . .). In making such a comparison, however, one must be sensitive to the limitations of the current R formulation. Generally, one should not expect a good correlation between the model and observational results unless the environmental conditions associated with a particular storm are within the range of environmental conditions associated with the model experiments. Since the environmental conditions associated with observed storms are con-

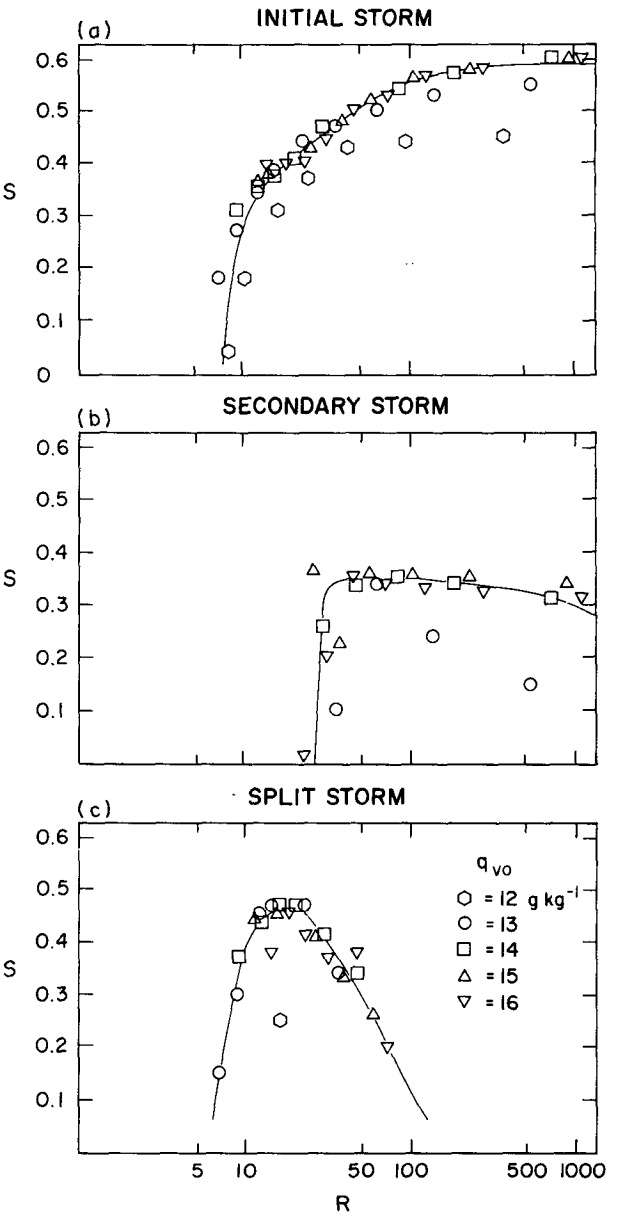

FIG. 13. Storm strength S versus R for (a) initial storms, (b) secondary storms and (c) split storms.

TABLE 1. Classification of documented convective storms.

Case	Date	Notes and documentation	Designation
S1	9 July 1959	"Wokingham storm" Thorpe and Miller (1978) Browning and Ludlum (1962)	supercell
S2	3 April 1964	Wilhelmson and Klemp (1981) Fujita and Grandoso (1968)	supercell
S3	19 April 1972	Brown *et al.* (1973)	supercell
S4	24 May 1973	"Union City tornado" Lemon *et al.* (1978)	supercell
S5	8 June 1974	"Harrah storm" Ray (1976), Heymsfield (1978) Brandes (1977)	supercell
S6	20 May 1977	Klemp *et al.* (1981)	supercell
S7	10, 11 April 1979	"Wichita Falls"* Alberty *et al.* (1979)	supercell
S8	2 May 1979	Alberty *et al.* (1979)	supercell
S9	Mean sounding	Fankhauser and Mohr (1977)	long-lived cells
BK	13 June 1976	Iowa cyclonic-anticyclonic tornado pair Brown and Knupp (1980)	?
M1	Mean sounding	Fankhauser and Mohr (1977)	multicell
M2	9 July 1973	"Raymer" storm Chen (1980)	multicell
M3	14 August 1975	"Hampstead" storm Thorpe and Miller (1978) Miller (1978)	multicell
M4 M5	19 August 1975 20 August 1975	Thunderstorms observed during Florida Area Cumulus Experiment (FACE) Brown (1978)	unorganized multicells
TR1 TR2 TR3 TR4	—	Soundings characteristic of the tropical environments**	tropical cloud clusters and squall lines

* Soundings of temperature and moisture estimated by Dr. Fred Sanders. Winds estimated by author.
** Soundings supplied by Dr. Edward Zipser (NCAR).

siderably more complex and varied than those in the model, application of these results to observations must be viewed with caution.

With this in mind, the single cell, multicell and supercell storm cases are each plotted versus R in Fig. 14. The range of model results is included above the observational cases. Note the strong correlation with the model results for most of the supercell and multicell cases considered. In particular, most of the tornadic supercell cases fall within an R range of 15–35 which fits quite well with the optimal conditions indicated for the modeled split storms. Multicells, on the other hand, occurred for R generally greater than 40, also in agreement with the model results.

One exception to the above tendencies is the Brown and Knupp storm which was not given a classification in Table 1. This case has a value of R ($\sim$125) which would clearly suggest multicell characteristics based on the model results, but which also produced a series of strong long-lived tornadoes. Such an observation is usually attributed to supercell type storms. Brown (personal communication), however, has classified the storm as unsteady over much of its lifetime, a characteristic often attributed to multicell type structures. Also, the buoyant energy associated with this storm was estimated to be over 5000 $m^2 s^{-2}$, which is much larger than that considered in the model experiments. Our general concepts of storm classification (whether based on model or observational results) may not work in cases such as this.

Of special significance in this comparison are the values of R for the composite soundings of Fankhauser and Mohr (1977) for multicell and long-lived storms. These soundings represent mean conditions

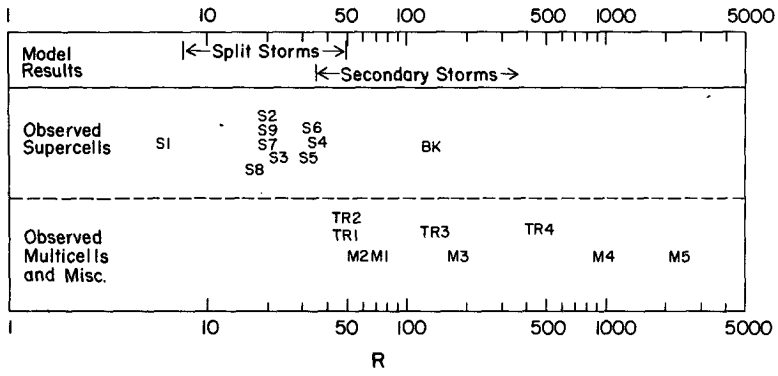

FIG. 14. R calculations for storms included in Table 1.

taken over many cases under many different conditions, and may represent statistically more meaningful environmental conditions. Both the long-lived storms (which we roughly equate to the model supercells) ($R = 20$) and the multicell storms ($R = 70$) have values of R which match the model results well.

The storms used in the above comparison cover a wide range of environmental conditions, but still only represent a very small sample. Work is underway to increase this sample size, but for the present, any conclusions drawn from this comparison must be considered quite preliminary.

6. Summary and conclusions

The dependence of convective storm structure on environmental wind shear and buoyancy has been investigated through the use of the Klemp-Wilhelmson three-dimensional numerical cloud model. Storms have been initiated in a horizontally homogeneous environment characterized by an available buoyant energy [defined by Eq. (3)] which ranges from 1000–3500 $m^2 s^{-2}$ and one-dimensional low-level vertical wind shears which range from 0 through 0.008 s^{-1}. The results suggest the ability of the model to produce a spectrum of storm types qualitatively similar to what is observed in nature. In particular, for a given amount of buoyancy, weak shear produces short-lived single cells, low-to-moderate shears produce secondary developments similar to observed multicells, while moderate-to-high shears produce split storms which are the model equivalent of the observed supercells. Variations in the available buoyant energy modulate this storm spectrum in a manner which suggests that a ratio of buoyant energy to vertical wind shear is important in determining the basic features of the particular storm structures. In addition, an optimal wind shear-buoyancy condition exists for the development of supercell type storms.

The relationship between wind shear and buoyancy has been expressed in terms of a nondimensional convective parameter R which delineates the various storm regimes for the range of experimental conditions considered. Comparison of the model results to calculations of R for documented severe storm cases are quite favorable, suggesting not only the ability of the model to simulate at least the qualitative aspects of observed modes of convection, but also the ability of the R formulation to suggest the environmental conditions most favorable for particular storm types in the real world.

Many limitations of the above results have been noted, in particular the relatively small range of environmental conditions used in the model experiments as compared to the range found in nature and uncertainties associated with model storm initiation. Work is now underway or planned to expand the model realm of conditions to consider such effects as directionally varying wind shears, different profiles of temperature and moisture, and the effects of horizontal inhomogeneities such as mesoscale forcing or thermal boundaries. In addition, studies are planned to delve more into the details of the dynamics of the various storm structures to determine what mechanisms decide whether split or secondary type developments will occur in a particular wind shear-buoyancy regime.

Additional studies will certainly modify many of the quantitative results suggested in this initial study. Refinements in our knowledge of the effects of wind shear and buoyancy on storm structure would hopefully improve the manner in which the convective parameter R is calculated, and more clearly define the range of environmental conditions for which this parameter may be meaningful. For example, the current formulation may not be applicable to tropical systems or cases where mesoscale features play an important role in storm initiation and evolution. However, the fact that this limited series of model experiments suggests a wind shear-buoyancy relationship for storm structure which qualitatively agrees with an uncontrolled set of observations is an encouraging sign that the great complexity of convective storm evolution may be largely governed by

a limited number of observable features of the environment.

Acknowledgments. The authors wish to express their gratitude to Dr. Richard Rotunno and Dr. Douglas Lilly at NCAR, Dr. Bob Wilhelmson at the University of Illinois, and Dr. John Brown at NOAA for the many helpful discussions concerning this work. We would also like to thank Dorene Howard at NCAR for typing the manuscript.

REFERENCES

Alberty, R. L., D. W. Burgess, C. E. Hane and J. F. Weaver, 1979: SESAME 1979 Operations Summary. NOAA ERL, Boulder, CO, August 1979, 253 pp. [U.S. Government Printing Office 1979, 677-072/1303, Reg. 8. Dr. Ronnie L. Alberty, Mail Code RX6, 325 S. Broadway, Boulder, CO 80303].

Brandes, E. A., 1977: Gust front evolution and tornadogenesis as viewed by Doppler radar. *J. Appl. Meteor.*, **19,** 333–338.

Brown, J. M., 1978: Water budget of cumulonimbus clusters and of the peninsular scale over south Florida. Final report, NOAA Grant 04-7-022-44030, 187 pp. [NTIS PB-293 590-69A].

——, and K. R. Knupp, 1980: The Iowa cyclonic-anticyclonic tornado pair and its parent thunderstorm. *Mon. Wea. Rev.*, **108,** 1626–1646.

Brown, R. A., D. W. Burgess and K. C. Crawford, 1973: Twin tornado cyclones within a severe thunderstorm: Single Doppler radar observations. *Weatherwise*, **26,** 63–71.

Browning, K. A., 1964: Airflow and precipitation trajectories within severe local storms which travel to the right of the winds. *J. Atmos. Sci.*, **21,** 634–639.

——, 1977: The structure and mechanism of hailstorms. *Meteor. Monogr.*, No. 38, Amer. Meteor. Soc., 1–39.

——, and F. H. Ludlam, 1962: Airflow in convective storms. *Quart. J. Roy. Meteor. Soc.*, **88,** 117–135.

Byers, H. R., and R. R. Braham, Jr., 1949: *The Thunderstorm.* U.S. Government Printing Office, Washington, DC, 287 pp.

Chen, C.-S., 1980: The effect of the gust front on the generation of new convection. Ph.D. thesis, University of Illinois, 192 pp.

Chisholm, A. J., and J. H. Renick, 1972: The kinematics of multicell and supercell Alberta hailstorms. Alberta hail studies, Research Council of Alberta Hail Studies, Rep. 72-2, 24-31, 53 pp.

Fankhauser, J. C., and C. G. Mohr, 1977: Some correlations between various sounding parameters and hailstorm characteristics in northeast Colorado. *Preprints 10th Conf. Severe Local Storms*, Omaha, Amer. Meteor. Soc., 218–225.

Fawbush, E. J., and R. C. Miller, 1954: The types of airmasses in which North American tornadoes form. *Bull. Amer. Meteor. Soc.*, **35,** 154–165.

Foote, G. B., 1977: Response to "The structure and mechanism of hailstorms", *Meteor. Monogr.*, No. 38, 45–47.

Fujita, T., and H. Grandoso, 1968: Split of a thunderstorm into anticyclonic and cyclonic storms and their motion as determined from numerical model experiments. *J. Atmos. Sci.*, **25,** 416–439.

Heymsfield, G. M., 1978: Kinematic and dynamic aspects of the Harrah tornadic storm analyzed from dual-Doppler radar data. *Mon. Wea. Rev.*, **106,** 233–254.

Klemp, J. B., and R. B. Wilhelmson, 1978a: The simulation of three-dimensional convective storm dynamics. *J. Atmos. Sci.*, **35,** 1070–1096.

——, and ——, 1978b: Simulations of right- and left-moving storms produced through storm splitting. *J. Atmos. Sci.*, **35,** 1097–1110.

——, —— and P. S. Ray, 1981: Observed and numerically simulated structure of a mature supercell thunderstorm. *J. Atmos. Sci.*, **38,** 1558–1580.

Lemon, L. R., 1980: Severe thunderstorm radar identification techniques and warning criteria. NOAA Tech. Memo. NWS NSSFC-3, NSSL, Kansas City, 60 pp. [U.S. Department of Commerce, Sills Building, 5285 Port Royal Road, Springfield, VA 22151].

——, and C. A. Doswell III, 1979: Severe thunderstorm evolution and mesocyclone structure as related to tornadogenesis. *Mon. Wea. Rev.*, **107,** 1184–1197.

——, D. W. Burgess and R. A. Brown, 1978: Tornadic storm airflow and morphology derived from single-Doppler radar measurements. *Mon. Wea. Rev.*, **106,** 48–61.

Lilly, D. K., 1979: The dynamical structure and evolution of thunderstorms and squall lines. *Annual Review of Earth and Planetary Science*, Vol. 7, Annual Reviews, Inc., 117–161.

Maddox, R. A., 1976: An evaluation of tornado proximity wind and stability data. *Mon. Wea. Rev.*, **104,** 133–142.

Marwitz, J. D., 1972a: The structure and motion of severe hailstorms. Part I: Supercell storms. *J. Appl. Meteor.*, **11,** 166–179.

——, 1972b: The structure and motion of severe hailstorms. Part II: Multi-cell storms. *J. Appl. Meteor.*, **11,** 180–188.

——, 1972c: The structure and motion of severe hailstorms. Part III: Severely sheared storms. *J. Appl. Meteor.*, **11,** 189–201.

Miller, M. J., 1978: The Hampstead storm: A numerical simulation of a quasi-stationary cumulonimbus system. *Quart. J. Roy. Meteor. Soc.*, **104,** 413–427.

Moncrieff, M. W., 1978: The dynamical structure of two-dimensional steady convection in constant vertical shear. *Quart. J. Roy. Meteor. Soc.*, **104,** 543–567.

——, and J. S. A. Green, 1972: The propagation and transfer properties of steady convective overturning in shear. *Quart. J. Roy. Meteor. Soc.*, **98,** 336–352.

——, and M. J. Miller, 1976: The dynamics and simulation of tropical cumulonimbus and squall lines. *Quart. J. Roy. Meteor. Soc.*, **102,** 373–394.

Newton, C. W., and J. C. Fankhauser, 1975: Movement and propagation of multicellular convective storms. *Pure Appl. Geophys.*, **113,** 747–764.

Pastushkov, R. S., 1975: The effects of vertical wind shear on the evolution of convective clouds. *Quart. J. Roy. Meteor. Soc.*, **101,** 281–291.

Ray, P. S., 1976: Vorticity and divergence fields within tornadic storms from dual-Doppler observations. *J. Appl. Meteor.*, **15,** 879–890.

Rotunno, R., 1981: On the evolution of thunderstorm rotation. *Mon. Wea. Rev.*, **109,** 171–180.

Schlesinger, R. E., 1978: A three-dimensional numerical model of an isolated thunderstorm. Part I: Comparative experiments for variable ambient wind shear. *J. Atmos. Sci.*, **35,** 690–713.

——, 1980: A three-dimensional numerical model of an isolated thunderstorm. Part II: Dynamics of updraft splitting and mesovortex couplet evolution. *J. Atmos. Sci.*, **37,** 396–420.

——, 1982: Effects of mesoscale lifting, precipitation and boundary-layer shear on severe storm dynamics in a three-dimensional numerical modeling study. *Preprints 12th Conf. Severe Local Storms*, San Antonio, Amer. Meteor. Soc., 536–541.

Thorpe, A. J., and M. J. Miller, 1978: Numerical simulations showing the role of the downdraught in cumulonimbus motion and splitting. *Quart. J. Roy. Meteor. Soc.*, **104,** 873–893.

Tripoli, G. J., and W. R. Cotton, 1980: A numerical investigation of several factors contributing to the observed variable intensity of deep convection over south Florida. *J. Appl. Meteor.*, **19,** 1037–1063.

Wilhelmson, R. B., and J. B. Klemp, 1978: A numerical study of storm splitting that leads to long lived storms. *J. Atmos. Sci.*, **35,** 1974–1986.

——, and ——, 1981: A three-dimensional numerical simulation of splitting severe storms on 3 April 1964. *J. Atmos. Sci.*, **38,** 1581–1600.